ACS OMEGA

Article

Cite This: ACS Omega 2019, 4, 8731−8738

http://pubs.acs.org/journal/acsodf

Temperature-Induced Single-Crystal-to-Single-Crystal Transformations with Consequential Changes in the Magnetic Properties of Fe(III) Complexes

Amit Adhikary,*[,†] Sohel Akhtar,[†] Anand Pariyar,[‡] Andrei S. Batsanov,[§] and Raju Mondal*[,†]

[†]School of Chemical Sciences, Indian Association for the Cultivation of Science, 2A &2B, Raja S. C. Mullick Road, Kolkata 700032, West Bengal, India

[‡]Department of Chemistry, Sikkim University, Sikkim 737102, India

[§]Department of Chemistry, University of Durham, South Road, Durham, DH1 3LE, U.K.

Supporting Information

ABSTRACT: The present article deals with an one-to-one structure−property correspondence of a dinuclear iron complex, $[Dipic(H_2O)FeOH]_2{\cdot}H_2O$ (**1**) (Dipic = pyridine-2,6-dicarboxylic acid). Variable-temperature X-ray single-crystal structural analysis confirms a phase transition of complex **1** to complex **2** ($[Dipic(H_2O)FeOH]_2$) at 120 °C. Further, single-crystal-to-single-crystal (SCSC) transformation was monitored by temperature-dependent single crystal X-ray diffraction, powder X-ray diffraction, time-dependent Fourier-transform infrared spectroscopy, and differential scanning calorimetry. SCSC transformation brings the change in space group of single crystal. Complex **1** crystallizes in the $C2/c$ space group, whereas complex **2** crystallizes in the $P\bar{1}$ space group. SCSC transformation brings the change in packing diagram as well. Complex **1** shows two-dimensional network through H-bonding, whereas the packing diagram of complex **2** shows a zigzag-like arrangement. Phase transformation not only fetches structural changes but also in the magnetic properties. Difference in Fe−O−Fe bond angles of two complexes creates notable variation in their antiferromagnetic interactions with adjacent metal centers.

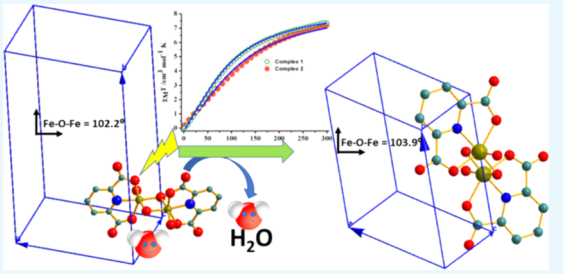

INTRODUCTION

Single-crystal-to-single-crystal (SCSC) transformation of coordination complex with irretrievable changes of properties may lead to the development of innovative materials.[1−3] This is particularly true for magnetic materials as subtle modification in the metal−ligand environment can have a profound impact on their superexchange pathway, the all-important mode of magnetic interaction.[2,4] Such tuning of magnetic interaction needs to ensure that structural integrity remains intact after SCSC transformation. Most of the SCSC transitions are induced by light, heat, and guest removal, especially solvents, which often lead to collapse of the compound. Key to a successful maneuvering of magnetic properties via SCSC transformation therefore lies in retaining the structural integrity of the system.[5,6] On the other hand, tuning the magnetic properties sensitive to guest molecule is attracting interest because of their various potential applications such as magnetic sponge[7−9]switches, sensors, etc.[10,11]Notwithstanding, only a limited number of SCSC transformations without changing the coordination sphere of the metal center are known in the literature.[11−17] Although, most of these compounds showed spin crossover behavior. To successfully implement of SCSC transformation, appropriate ligands must be used. Among the vast variety of organic ligands that can be used for SCFs, dicarboxylates are good candidates having potential donor sites. Symmetrical pyridine-2,6-dicarboxylic acid (Dipic) having five potential donor atoms can have various coordination modes,[15] especially with iron metal ion due to strong Fe−O bond.[18,19] Although Fe−Dipic complex is known for many years, their structural and magnetic properties are still not clearly understood. Here, we report a structure of complex **1** having formula, $[Dipic(H_2O)FeOH]_2{\cdot}H_2O$, which, upon heating at 120 °C, transformed to complex **2** having formula $[Dipic(H_2O)FeOH]_2$.[20] This structural transformation was induced by removal of lattice water molecules, while temperature acts as an external stimulus. Transformation also brings the change in bond distance and bond angle. The Fe−O−Fe bond angle, which is a crucial parameter of magnetic exchange, was also changed. As a consequence, magnetic studies display their difference in magnetic interactions, revealing from the coupling constant (J). Complex **1** shows a J value of −13.2 cm^{-1}, and complex **2** shows a J value of −16.2 cm^{-1}.

Received: December 4, 2018
Accepted: April 30, 2019
Published: May 22, 2019

DOI: 10.1021/acsomega.8b03400
ACS Omega 2019, 4, 8731−8738

RESULTS AND DISCUSSION

Synthesis. Complex **1** was synthesized by the layering technique using $Fe(ClO_4)_2{\cdot}xH_2O$ and Dipic in H_2O/MeOH solvent mixture. Using different anions of Fe(II) salts as well as different Fe(III) salts, complex **1** was also formed. Complex **2** was formed by heating complex **1** at ∼120 °C for few hours.

Structural Description. The crystallographic parameters of both the complexes are compared in Table 1. Complex **1** crystallizes in the $C2/c$ space group, whereas complex **2** crystallizes in the $P\bar{1}$ space group (Figure 1). Both the complexes contain two Dipic, two Fe(III) ions, two coordinated water, and two μ-OH^-. In addition, complex **1** has one H_2O molecule as solvent (Figure 2). Each Fe(III) center of both the complexes has distorted octahedral geometry having N_1O_5 coordination.

Each Fe(III) center is coordinated by two O atoms of two carboxylate groups, two −OH groups, and one H_2O and N atom of the pyridine ring. Two Fe(III) ions are bridged by two μ-OH groups and form a diamond-shaped four-membered ring. An inversion center passes through the center of the ring. Polyhedral views of both the complexes are shown in Figure 3. Adjacent polyhedra are connected through edge sharing. Differences in the bond distances of the two complexes are compared in Figure 3. Fe−O−Fe bond angles are 102.2 and 103.9° for complexes **1** and **2**, respectively. The Fe−Fe bond distance is 3.065(3) Å for complex **1** and 3.095(1) Å for complex **2**. The Fe−O bond distance is in the range of 1.97(6)−2.09(8) Å for complex **1** and 1.89(4)−2.07(4) Å for complex **2**. The Fe−N bond distance is 2.07(7) Å for complex **1** and 1.98(5) Å for complex **2**. There are several H-bonding interactions in both the complexes (Figure 4). However, for complex **1**, H-bonding is further increased due to participation of H_2O molecule. If we closely see the dimeric unit of both the complexes, the distance between two molecular units increases

Table 1. Comparison of the Crystallographic Parameters of Complexes 1 and 2

complex	complex 1	complex 2
empirical formula	$C_{14}H_{14}Fe_2N_2O_{13}$	$C_{14}H_{12}Fe_2N_2O_{12}$
formula weight	529.97	511.91
T/K	293	293
wavelength/Å	0.71073	0.71073
crystal system	monoclinic	triclinic
space group	$C2/c$	$P\bar{1}$
a/Å	11.383(3)	7.251(2)
b/Å	21.696(9)	8.010(3)
c/Å	7.452(3)	8.795(2)
α/deg	90	82.18(1)
β/deg	90.22(1)	70.18(7)
γ/deg	90	64.89(7)
volume/Å^3	1840.23(1)	435.1(2)
Z	4	1
ρ_{calc}/Mg m^{-3}	1.884	1.931
μ/mm^{-1}	1.653	1.741
goodness of fit (S)	1.182	1.244
R [$I > 2\sigma(I)$][a]	0.0133	0.0517
wR (F^2) (all data)[b]	0.0245	0.1316
δF/e Å^{-3}	0.343, −0.402	0.475, −0.819
CCDC no.	1866848	1866851

[a] $R_1 = \sum||F_o|-|F_c||/\sum|F_o|$. [b] $wR_2 = \{\sum[w(F_o^2 - F_c^2)^2]/\sum[w(F_o^2)^2]\}^{1/2}$, $w = 1/[\sigma^2(F_o)^2 + (aP)^2 + bP]$, where $P = [F_o^2 + 2F_c^2]/3$.

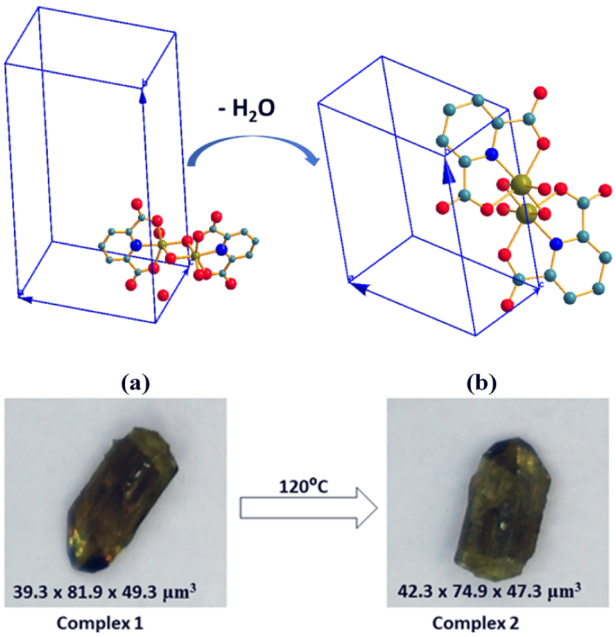

Figure 1. Unit cell of complexes **1** (a) and **2** (b). Color code: Fe, dark yellow; C, gray; N, blue; O, red. (c) Transformation of single crystal of complex **1** to complex **2**.

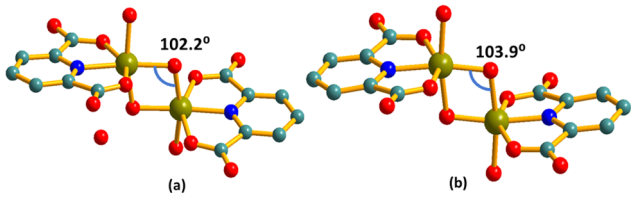

Figure 2. Molecular structure of complex **1** (a) and complex **2** (b). H atoms are omitted for clarity.

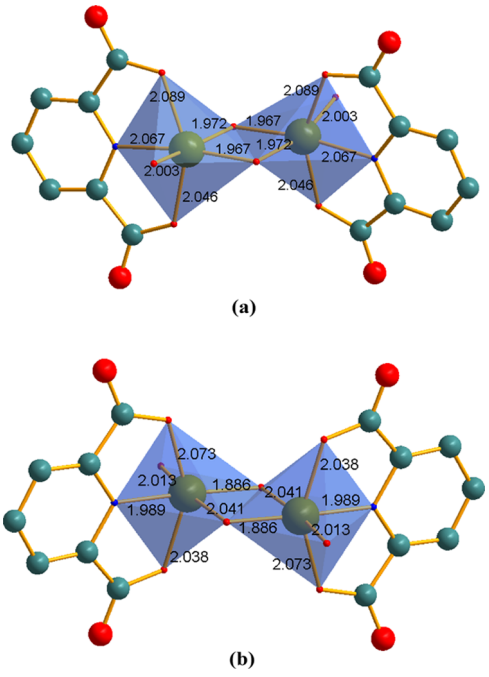

Figure 3. (a) Polyhedra of complex **1** and (b) polyhedra of complex **2**, illustrating edge sharing between the two polyhedra. Bond distances are shown in Å.

DOI: 10.1021/acsomega.8b03400
ACS Omega 2019, 4, 8731−8738

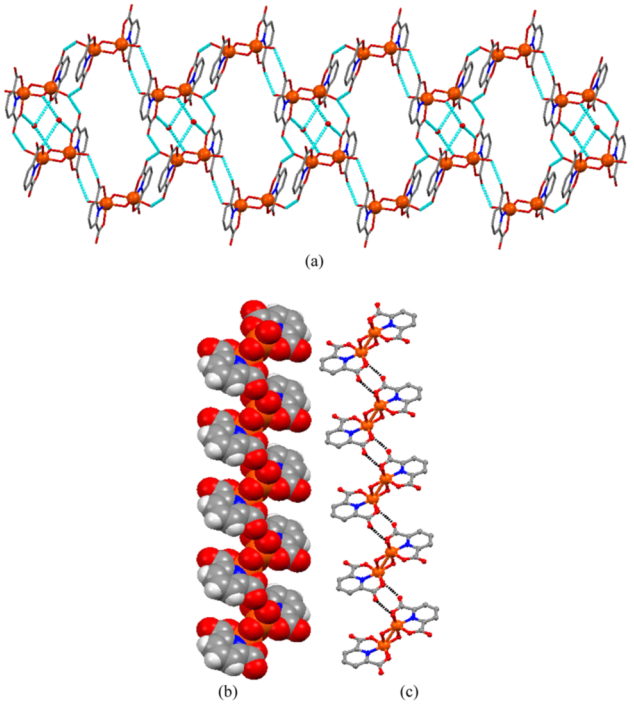

Figure 4. (a) Packing diagram of complex **1** along *c*-axis, through extensive H-bonding network. (b) Space-fill representation of zigzag arrangement of complex **2** along *a*-axis. (c) Zigzag packing representation of complex **2** through H-bonding.

from complex **1** to complex **2** (Figure 5). Complex **1** has an intermolecular distance of 7.452 Å, which is increased to 8.795

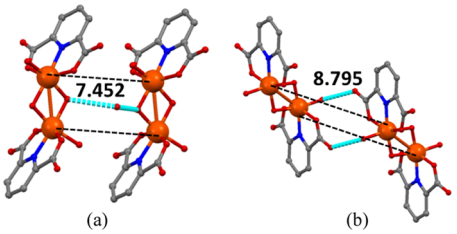

Figure 5. H-bonded dimeric unit of (a) complex **1** and (b) complex **2**.

Å for complex **2**. So, the H_2O molecule helps to bring two molecular units more closely. Therefore, in the absence of H_2O, the intermolecular distance increases. Interestingly, an intermolecular distance of 7.452 Å is unit cell length "*c*" of complex **1** and an intermolecular distance of 8.795 Å is unit cell length "*c*" of complex **2**. Therefore, H-bonding is very crucial for change of unit cell parameters. The packing diagram of complex **2** shows zigzag-like arrangement (Figure 4b,c), whereas for complex **1**, the packing diagram is completely different because of the difference in H-bonding. For complex **1**, H_2O molecules reside in between the dinuclear units (Figure 4a). SCSC transformation further affects the $\pi-\pi$ interactions. In complex **1**, the distance between two centroids of $\pi-\pi$ interaction is 3.621 Å, whereas after the transformation, phenyl rings come closer and the distance between two centroid of $\pi-\pi$ interaction decreases to 3.456 Å (Figure 6).

Hirshfeld Surface Analysis. Hirshfeld surface analysis was carried out to study the nature of intra- and intermolecular interactions for difference in the packing diagram. Our focus

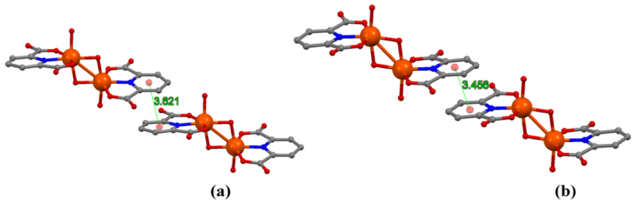

Figure 6. $\pi-\pi$ interactions of (a) complex **1** and (b) complex **2**.

here is on the O···H and N···H interactions. The N−H···H and O−H···H interactions are distinguished on the basis of charge density. A large number of red zones in the d_{norm} of Hirshfeld surface area represent the presence of significant short interactions for both the complexes, and intermolecular hydrogen-bonding interactions of complexes **1** and **2** are shown in Figure 7a,d, respectively. Contributions of intermolecular interactions of O···H and N···H to the total Hirshfeld surface area are shown in Figure 7. The O···H interactions comprise 15.4% to the total Hirshfeld surface area in complex **1**, whereas the percentage of O···H interactions increases to 16.3% in complex **2**. N···H interactions comprise only 0.2% to the total Hirshfeld surface area in complexes **1** and **2**, and N···H interactions comprise 0.4%. Therefore, such difference in O···H and N···H interactions of both the complexes significantly affects the packing diagram and displays drastic changes in the packing.

Temperature-Dependent Single-Crystal XRD Study. Although two distinctly different forms were observed after heating at 120 °C, detailed variable-temperature diffraction studies were carried out to probe this phase transition. Accordingly, X-ray diffraction data for a single crystal were collected at 120, 170, 220, 270, and 320 K (Table 2). All of these structures confirmed the retention of complex **1** form. Unfortunately, the crystal started developing a crack at ca. 370 K. At 370 K, the same cell (complex **1**) was indexed, but intensities were not good enough for structure elucidation. The cracks get even bigger at 400 K, and it was not possible to index. Notwithstanding, from this original crystal, we managed to separate a small piece, suitable for diffraction. It was really gratifying to note that the structure obtained from this piece of crystal is indeed that of complex **2**, and henceforth confirms the SCSC transition or more precisely single-crystal-to-single-crystal phase transition.

Temperature-Dependent Powder X-ray Diffraction (PXRD) Study. To eliminate any ambiguity, a variable-temperature PXRD study was also carried out to monitor the phase transition of complex **1** to **2** (Figure 8). The PXRD patterns are highly corroborative to single-crystal data. At room temperature, the experimental PXRD pattern of complex **1** matches well with the simulated pattern.

Detailed investigation reveals that as the temperature increased, systematic changes appeared in the PXRD profile. Certain characteristic peaks for complex **1** diminish and new peaks generate for complex **2** at 130 °C. Three distinct peaks at 2θ = 8.2, 8.8, and 18.8° of complex **1** vanished with increasing temperature, whereas new peaks generated at 2θ = 10.8 and 12.3° at high temperature for the generation of complex **2**. At 160 °C, the PXRD pattern of the heated sample of complex **1** matches well with the simulated pattern of complex **2**. A slight discrepancy of peak at 29.3° may originate from inhomogeneity of the size of crystalline materials. So, from the

DOI: 10.1021/acsomega.8b03400
ACS Omega 2019, 4, 8731−8738

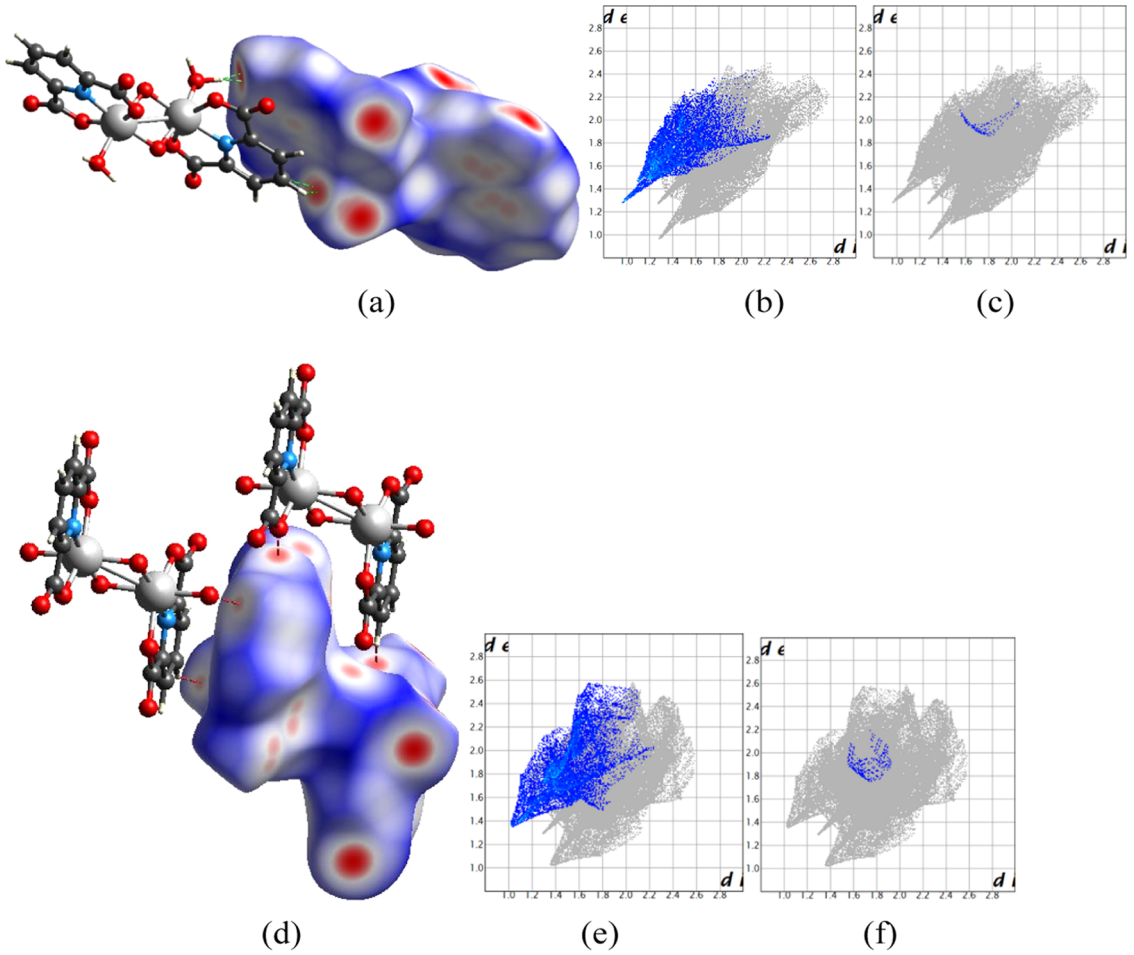

Figure 7. (a, d) Hirshfeld surface of complexes **1** and **2**, respectively (d_{norm}), showing the short contacts at the sites of H-bonding.[21] (b, e) Fingerprints of the O···H intermolecular interactions of complexes **1** and **2**, respectively. (c, f) N···H interactions of complexes **1** and **2**, respectively, within the crystal packings from the single-crystal X-ray diffraction data in complexes **1** and **2**, respectively. The gray zones represent all of the interactions, and the blue zones account for the corresponding O···H and N···H interactions.

Table 2. Summary of Crystallographic Parameters of Complex 1 at Different Temperatures

complex	complex 1 @120 K	complex 1 @170 K	complex 1 @220 K	complex 1 @270 K	complex 1 @320 K	complex 2 @370 K
empirical formula	$C_{14}H_{14}Fe_2N_2O_{13}$	$C_{14}H_{14}Fe_2N_2O_{13}$	$C_{14}H_{14}Fe_2N_2O_{13}$	$C_{14}H_{14}Fe_2N_2O_{13}$	$C_{14}H_{14}Fe_2N_2O_{13}$	$C_{14}H_{12}Fe_2N_2O_{12}$
formula weight	529.97	529.97	529.97	529.97	529.97	511.91
T/K	120	170	220	270	320	293
wavelength/Å	0.71073	0.71073	0.71073	0.71073	0.71073	0.71073
crystal system	monoclinic	monoclinic	monoclinic	monoclinic	monoclinic	triclinic
space group	$C2/c$	$C2/c$	$C2/c$	$C2/c$	$C2/c$	$P\bar{1}$
a/Å	11.479(5)	11.466(4)	11.434(3)	11.443(4)	11.438(3)	7.251(2)
b/Å	21.724(6)	21.729(6)	21.726(7)	21.738(6)	21.752(8)	8.010(3)
c/Å	7.354(3)	7.388(3)	7.419(3)	7.457(3)	7.487(3)	8.795(2)
α/deg	90	90	90	90	90	82.18(1)
β/deg	90.18(3)	90.066(3)	89.963(3)	89.899(3)	89.810(3)	70.18(7)
γ/deg	90	90	90	90	90	64.89(7)
volume/Å^3	1833.85(1)	1840.34(1)	1843.13(1)	1854.97(1)	1862.74(1)	435.1(2)
Z	4	4	4	4	4	1
ρ_{calc}/Mg m^{-3}	1.920	1.913	1.910	1.898	1.890	1.931
μ/mm^{-1}	1.660	1.654	1.652	1.641	1.634	1.741
goodness of fit (S)	1.046	1.058	1.063	1.080	1.042	1.244
R $[I > 2\sigma(I)]$[a]	0.0353	0.0322	0.0346	0.0341	0.0353	0.0517
wR (F^2) (all data)[b]	0.0836	0.080	0.0914	0.0855	0.0900	0.1316
δF/e Å^{-3}	0.412, −0.546	0.427, −0.384	0.410, −0.414	0.419, −0.444	0.328, −0.442	0.475, −0.819
CCDC no.	1866854	1866852	1866849	1866850	1866853	1866851

[a] $R_1 = \sum||F_o|-|F_c||/\sum|F_o|$. [b] $wR_2 = \{\sum[w(F_o^2 - F_c^2)^2]/\sum[w(F_o^2)^2]\}^{1/2}$, $w = 1/[\sigma^2(F_o)^2 + (aP)^2 + bP]$, where $P = [F_o^2 + 2F_c^2]/3$.

DOI: 10.1021/acsomega.8b03400
ACS Omega 2019, 4, 8731−8738

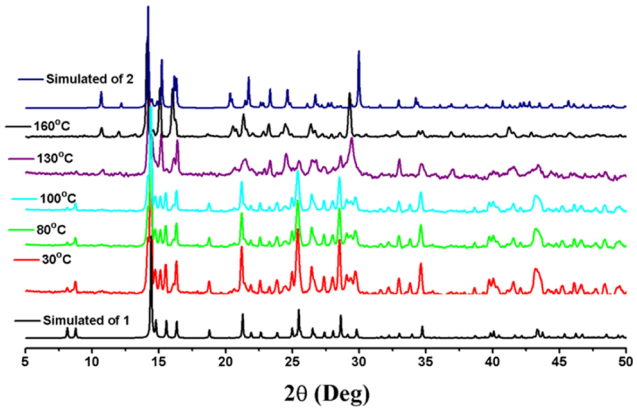

Figure 8. Simulated and temperature-dependent experimental X-ray powder diffraction patterns observed from the sample of complex **1**.

temperature-dependent PXRD study, the transformation of complex **1** to complex **2** upon heating is clearly visible.

Fourier-Transform Infrared (FT-IR) Study. To further support the change of structural transformation of complex **1** to **2**, temperature-dependent FT-IR study was carried out. It is interesting to examine the change of O−H stretching frequency of H_2O molecule with temperature. Complex **1** has a broad O−H stretching frequency at ∼3487 cm^{-1} and bending of two doublets at 1643 and 1652 cm^{-1}.

Conversely, complex **2** has a broad O−H stretching frequency at ∼3413 cm^{-1} and bending of two doublets at 1620 and 1654 cm^{-1}. Complex **1** was heated at the temperature of 120 °C for 12 h and FT-IR spectra were measured. The FT-IR spectrum of the heated sample well matched with that of complex **2** (Figure 9). Furthermore,

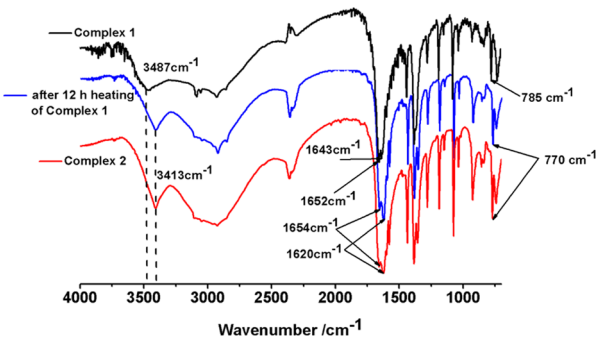

Figure 9. Comparison of FT-IR spectra of complex **1**, complex **1** after heating, and complex **2**.

complex **1** was heated at the temperature of 120 °C at different time intervals. After 6 h, there is a change of spectrum, as O−H stretching shifted from ∼3487 to 3413 cm^{-1} (Figure S1).

DSC Study. Thermal analysis was carried out for complex **1** by means of differential scanning calorimetry (DSC) at the rate of 5 °C/min. DSC measurements show one broad endothermic peak for complex **1** at ∼157 °C corresponding to a solid-to-solid phase transformation of complex **1** to **2**. Similar SCSC transformation and removal of H_2O molecules were also observed in the $[Mn_2(4\text{-Apha})_4(H_2O)_2]\cdot 2H_2O$[22] complex, where a broad peak at 161 °C was observed indicating the transformation. The cooling graph does not show any peak suggesting that the transformation is irreversible (Figure 10). The ΔH value of ∼17.2 kJ mol^{-1} was calculated

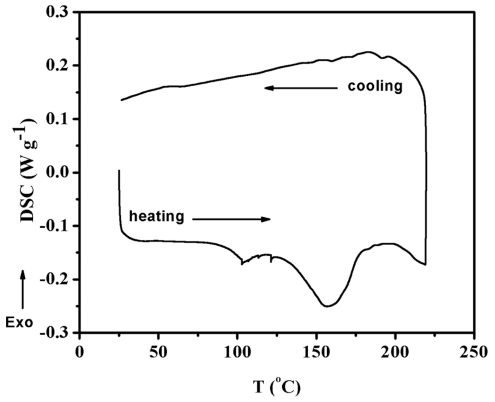

Figure 10. DSC thermogram of complex **1** at the rate of 5 °C/min.

from the DSC curve. If we consider removal of a H_2O molecule, it implies breaking of two H-bonds. Wendler et al. proposed that ΔH = 21.5 kJ mol^{-1} corresponds to breaking of two H-bonds.[23] So, the enthalpy is close to the experimental value. A similar change in enthalpy was also observed for the transformation of $[Cu(PDC)(py)_2C(OH)_2)(H_2O)]$ to $[Cu(PDC)(py)_2C(OH)_2)]$.[24] Further, DSC measurement was conducted at a lower temperature of 2 °C and a sharp peak was observed at ∼159 °C due to phase transformation (Figure S2). Thus, from the DSC curve, we also observed the clear transformation at 160 °C.

Void Space Calculation. To investigate the number of H_2O molecules and void space in the system, PLATON[25] software was used. No solvent-accessible void space was found for both the complexes. Further, void space was calculated for complex **1** after removing the H_2O molecule from unit cell, and there was a total void space of 92.4 $Å^3$, where only hydrogen-bonded H_2O can fit to occupy ∼40 $Å^3$ space. Therefore, in complex **1**, only one H_2O molecule is present. After removing the H_2O molecule, the complex became unstable in the monoclinic system because of the huge void space of 92.4 $Å^3$ and converted to triclinic system of complex **2**.

DFT Calculation. The loss of one H_2O molecule from the hydrogen-bonded system of complex **1** was expected to be compensated by means of structural rearrangement. Therefore, to investigate the energy aspects of structural transformation, single-point DFT calculations were performed using G09 program. Complex **2** was found to be stabilized by 24.89 kJ mol^{-1} relative to complex **1** (Figure 11). The relative difference of ∼25 kJ mol^{-1} of energy is not sufficient to break covalent bonds (BDE for C−C = 350 kJ mol^{-1}); however, they are sufficient to produce conformational change

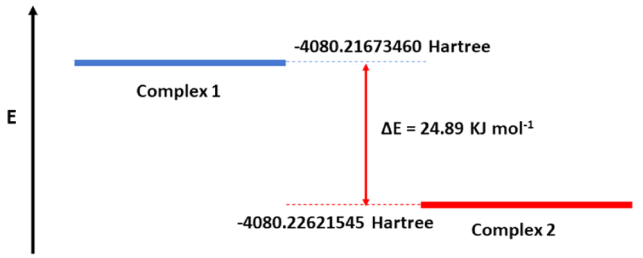

Figure 11. Energy level diagram of complexes **1** and **2**, calculated through single-point DFT calculation.

DOI: 10.1021/acsomega.8b03400
ACS Omega 2019, 4, 8731−8738

(ca. 2−3 kJ mol^{-1}) that is compensated by the loss of water molecules.

Magnetic Study. It is imperative to note here that the SCSC phase transition brings a significant change in the bond distance and angles related to the metals. Coincidentally, such change in bond distance and angles can bring about a profound change in their magnetic behavior. Naturally, we were interested in finding if the SCSC phase transition has any consequential change in magnetic behavior.

For magnetic characterization, dc susceptibility data were collected for complexes **1** and **2** on the polycrystalline sample in the temperature range of 2−300 K at 0.1 T. The observed room-temperature $\chi_M T$ (χ_M = molar magnetic susceptibility) values are 7.33 cm^3 mol^{-1} K for complex **1** and 7.22 cm^3 mol^{-1} K for complex **2**. Both the experimental $\chi_M T$ values are slightly lower than the theoretical $\chi_M T$ value of 8.75 cm^3 mol^{-1} K for two uncoupled Fe^{3+} and $g = 2$ probably due to the presence of antiferromagnetic interactions. With decreasing temperature, the $\chi_M T$ value gradually decreased and reached the minimum values of 0.02 and 0.23 cm^3 mol^{-1} K for complexes **1** and **2**, respectively, at 2 K (Figure 12). Decreasing the $\chi_M T$ value with

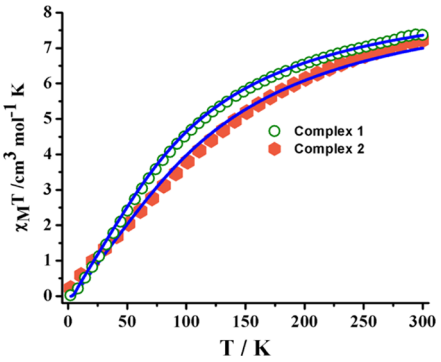

Figure 12. Temperature-dependent dc magnetic susceptibility of complexes **1** and **2**. The solid lines indicate fitting of the plots.

temperature is most probably due to the antiferromagnetic exchange between the adjacent Fe(III) centers. To study the magnetic interactions in detail, dinuclear model (Figure 13)

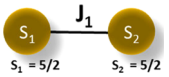

Figure 13. Model used for fitting of the $\chi_M T$ vs T plot for complex **1**.

was taken and fitted using the Hamiltonian (eq 1) and Van Vleck (eq 2) equations.

$$H = -JS_1S_2 - g\mu_B H \sum_{i=1}^{2} Si \quad (1)$$

[S = spin, J = intermolecular magnetic interaction]

$$\chi_{Fe2} = (N_A g^2 \mu_B{}^2/kT)\,[P/Q] \quad (2)$$

where $P = 2e^{2x} + 10e^{6x} + 28e^{12x} + 60e^{20x} + 110e^{30x}$ and $Q = 1 + 3e^{2x} + 5e^{6x} + 7e^{12x} + 9e^{20x} + 11e^{30x}$, $x = J/kT$.

$$\chi_M T = (\chi_{Fe2} T)/(1 - (zJ'\chi_{Fe2} T/N_A g^2 \beta^2)) \quad (3)$$

where zJ' denotes intermolecular magnetic interactions.

Best fitting of the plot resulted $J = -13.2$ cm^{-1} and $g = 2.03$ for complex **1** and $J = -16.2$ cm^{-1} and $g = 2.03$ for complex **2**. The negative values of J suggest antiferromagnetic interactions between two Fe(III) ions of both the complexes. In general, if the Fe−O−Fe angle is between ca. 93 and 98°, the interaction is ferromagnetic, and antiferromagnetic above that range.[26] For complex **1**, the Fe−O−Fe angle is 102.2°, and for complex 2, the Fe−O−Fe angle is 103.9°. So, the antiferromagnetic interaction is expected for both the complexes. However, because of the increase in the Fe−O−Fe angle for complex **2** compared to that for complex **1**, antiferromagnetic exchange is enhanced for complex **2**.

The J values of both the complexes are well comparable to the reported similar structure complex having two Fe(III) centers connected by μ-OH bridging, $[Chel(H_2O)FeOH]_2 \cdot 4H_2O$(chel = 4-hydroxo-2,6-pyridinedicarboxylate), where $J = -7.3$ cm^{-1}.[20]

Further, we consider intermolecular magnetic interactions (zJ') originated from various weak interactions, and the experimental $\chi_M T$ vs T plot was fitted using Van Vleck eqs 2 and 3[26] for both the complexes (Figure 14). From the best

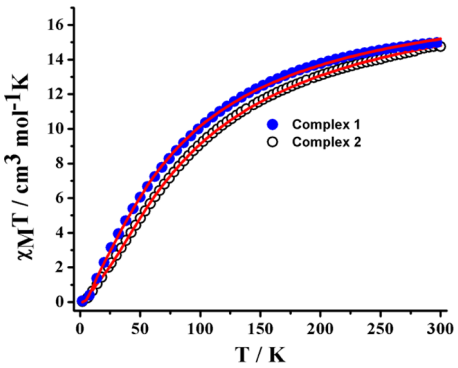

Figure 14. Temperature-dependent dc magnetic susceptibility of complexes **1** and **2**. The solid lines indicate fitting of the plots considering intermolecular interactions (zJ').

fitting, $J = -12.3$ cm^{-1}, $zJ' = -0.98$ cm^{-1}, and $g = 2.03$ were obtained for complex **1**. For complex **2**, $J = -15.4$ cm^{-1}, $zJ' = -1.1$ cm^{-1}, and $g = 2.03$ were obtained from the fitting. The negative zJ' value indicates very weak antiferromagnetic interactions. The values of zJ' interactions are very low for both the complexes due to very weak interactions.

Additionally, we have calculated energy of spins by fitting the $\chi_M T$ vs T plot using the FITMART software[27] considering isotropic interactions in matrix diagonalization process. From the plot, it has been observed that $S = 0$ is lowest in energy for both **1** and **2** (Figures S3 and S4). Therefore, ground-state spin of both the complexes are zero. Although, the difference in absolute energy values for the two complexes originate most probably due to difference in magnetic exchange.

Isothermal magnetization plots of complexes **1** and **2** at 2 K are shown in Figure S5. Both the complexes do not show any saturation even at the highest field of 7 T at 2 K due to the presence of antiferromagnetic interactions. Complex **1** shows maximum value of 0.06 Nβ, and complex **2** shows the maximum value of 0.061 Nβ at the field of 7 T. Both the values correspond to zero net spin.

CONCLUSIONS

In conclusion, we have successfully transformed one single crystal to another single crystal through solvent removal applying external heat as stimulus. PXRD, DSC, and FT-IR

DOI: 10.1021/acsomega.8b03400
ACS Omega 2019, 4, 8731−8738

studies clearly reveal the transformation. The change in crystal structure by phase transition has a direct effect on magnetism, which was explained in terms of the magnetic exchanges of complexes **1** and **2**. DFT calculation further endorses the SCSC transformation. Temperature-induced SCSC transition of similar systems is currently underway.

EXPERIMENTAL SECTION

Instrument. Infrared spectra were recorded in the solid state (KBr pellets) on a PerkinElmer FT-IR spectrometer in the range of 400−4000 cm^{-1}. Temperature-dependent FT-IR spectra were recorded using same pellet initially and after heating for 12 h at 120 °C. Additionally, FT-IR spectra were also recorded using new pellet after heating the sample for 12 h at 120 °C. The powder XRD patterns were obtained from a Rigaku instrument with Cu Kα anode, and measurements were done for the 2θ range of 5−50° with the scan rate of 0.025° s^{-1}. Variable-temperature PXRD data were recorded in aerobic condition. Variable-temperature direct current (dc) magnetic susceptibility data were collected on a quantum design MPMS SQUID VSM magnetometer equipped with a 0.1 T dc magnet and in the 2−300 K range. The measured values were corrected for the experimentally measured contribution of the sample holder, while the derived susceptibilities were corrected for the diamagnetism of the samples, estimated from Pascal's tables.[26]

X-ray Crystallography. X-ray crystallographic data for complexes **1** and **2** were collected on a Bruker Smart Apex 2 CCD diffractometer using graphite monochromated Mo Kα (λ = 0.71073) radiation. Data collections were performed using φ and ω scans. Data reduction and cell refinements were performed with the SAINT program,[28] and the absorption correction program SADABS[29] was employed to correct the data for absorption effects. The structure was solved using direct methods followed by full-matrix least-square refinements against F^2 (all data are in HKLF 4 format) using SHELXL-14.[30] Anisotropic refinement was used for all nonhydrogen atoms. Organic hydrogen atoms were placed in appropriate calculated positions. Variable-temperature single-crystal X-ray crystallographic data were collected on Agilent Technologies, Gemini S Ultra kappa-diffractometer. Refinements were done using SHELXL-15.[30] Short descriptions of crystal data are summarized in Table 1. X-ray crystallographic data in CIF format are available in CCDC 1866848−1866854.

DFT Calculation. All theoretical calculations were performed using the Gaussian 09 program.[31] DFT calculation employed the B3LYP functional using all electron basis sets. The geometry was fully optimized without symmetry constraints. All of the atoms are treated with double-ζ quality (DZVP) basis sets of 6-31G* quality.[32] Mulliken atomic charges of complexes **1** and **2** are given in Tables S1 and S2.

Synthesis. All of the chemicals and solvents were purchased from commercially available source and used without further purification.

Synthesis of [Dipic(H$_2$O)FeOH]$_2$· H$_2$O (1). Complex **1** was synthesized using the layering technique. A buffer layer of a 5 mL solution of H_2O/MeOH (1:1) was carefully layered over an aqueous solution (10 mL) of $Fe(ClO_4)_2 \cdot xH_2O$ (0.1 mmol). Then, a methanol/water (10:1) solution (5 mL) of the H_2Dipic (16.7 mg, 0.1 mmol) and NEt_3 (10.1 mg, 0.1 mmol) was carefully layered on top of the buffer layer. Orange-colored large single crystals were grown at the junction of the layers. All of the crystals were separated and washed with cold MeOH. Elemental analysis: ($C_{14}H_{14}Fe_2N_2O_{13}$): Calculated: C, 31.73; H, 2.66; N, 5.29. Found: C, 31.29; H, 2.54; N, 5.03.

ASSOCIATED CONTENT

Supporting Information

The Supporting Information is available free of charge on the ACS Publications website at DOI: 10.1021/acsomega.8b03400.

Time-dependent FT-IR spectra, isothermal magnetization, energy vs spin plot, DSC plot, and Mulliken atomic charges from DFT calculation (PDF)

Crystallographic data (CIF) (CIF) (CIF) (CIF) (CIF) (CIF) (CIF)

AUTHOR INFORMATION

Corresponding Authors

*E-mail: aadhikary87@gmail.com (A.A.).

*E-mail: icrm@iacs.res.in (R.M.).

ORCID

Amit Adhikary: 0000-0002-1435-4585

Andrei S. Batsanov: 0000-0002-4912-0981

Raju Mondal: 0000-0002-9013-7259

Notes

The authors declare no competing financial interest.

ACKNOWLEDGMENTS

R.M. gratefully acknowledges Science and Engineering Research Board (SERB) (Project No. EEQ/2018/000194), India, for financial support. AA acknowledges Science and Engineering Research Board (SERB) for national postdoctoral fellowship and financial support (order no. PDF/2016/000389). A.P. acknowledges SERB (EEQ/2016/000685) and DST-Inspire (DST/INSPIRE/04/2015/002674), Govt of India, for funding.

REFERENCES

(1) Duriska, M. B.; Neville, S. M.; Moubaraki, B.; Cashion, J. D.; Halder, G. J.; Chapman, K. W.; Balde, C.; Létard, J.-F.; Murray, K. S.; Kepert, C. J.; Batten, S. R. A Nanoscale Molecular Switch Triggered by Thermal, Light, and Guest Perturbation. *Angew. Chem., Int. Ed.* **2009**, *48*, 2549.

(2) Liu, J-L.; Wu, J-Y.; Huang, G-Z.; Chen, Y. C.; Jia, J-H.; Ungur, L.; Chibotaru, L. F.; Chen, X-M.; Tong, M-L. Desolvation-Driven 100-Fold Slowdown of Tunneling Relaxation Rate in Co(II)-Dy(III) Single-Molecule Magnets through a Single-Crystal to-Single-Crystal Process. *Sci. Rep.* **2015**, *5*, No. 16621.

(3) Chen, L.; Ye, J-W.; Wang, H. P.; Pan, M.; Yin, S. Y.; Wei, Z. W.; Zhang, L-Y.; Wu, K.; Fan, Y-N.; Su, C-Y. Ultrafast water sensing and thermal imaging by a metal-organic framework with switchable luminescence. *Nat. Commun.* **2017**, *8*, No. 15985.

(4) Zhang, Y-J.; Liu, T.; Kanegawa, S.; Sato, O. Reversible Single-Crystal-to-Single-Crystal Transformation from Achiral Antiferromagnetic Hexanuclears to a Chiral Ferrimagnetic Double Zigzag Chain. *J. Am. Chem. Soc.* **2009**, *131*, 7942.

(5) Ma, L.; Yang, J.; Lu, B. B.; Li, C. P.; Ma, J. F. Water-Stable Metal−Organic Framework for Effective and Selective $Cr_2O_7^{2-}$ Capture through Single-Crystal to Single Crystal Anion Exchange. *Inorg. Chem.* **2018**, *57*, 11746−11752.

(6) Kole, G. K.; Vittal, J. J. Solid-state reactivity and structural transformations involving coordination polymers. *Chem. Soc. Rev.* **2013**, *42*, 1755.

(7) Nishio, M.; Miyasaka, H. Magnetic Sponge Phenomena Associated with Interchain Dipole−Dipole Interactions in a Series

DOI: 10.1021/acsomega.8b03400
ACS Omega 2019, 4, 8731−8738

of Ferrimagnetic Chain Compounds Doped with Minor Diamagnetic Species. *Inorg. Chem.* **2014**, *53*, 4716.
(8) Zhang, J.; Kosaka, W.; Sugimoto, K.; Miyasaka, H. Magnetic Sponge Behavior via Electronic State Modulations. *J. Am. Chem. Soc.* **2018**, *140*, 5644.
(9) Kosaka, W.; Takahashi, Y.; Nishio, M.; Narushima, K.; Fukunaga, H.; Miyasaka, H. Magnetic Sponge with Neutral−Ionic Phase Transitions. *Adv. Sci.* **2018**, *5*, No. 1700526.
(10) Rodríguez-Jiménez, S.; Feltham, H-L.; Brooker, S. Non-Porous Iron(II)-Based Sensor: Crystallographic Insights into a Cycle of Colorful Guest-Induced Topotactic Transformations. *Angew. Chem., Int. Ed.* **2016**, *55*, 15067.
(11) Gentili, D.; Demitri, N.; Schafer, B.; Liscio, F.; Bergenti, I.; Ruani, G.; Ruben, M.; Cavallini, M. Multi-modal sensing in spin crossover compounds. *J. Mater. Chem. C* **2015**, *3*, 7836.
(12) Bartual-Murgui, C.; Codina, C.; Roubeau, O.; Aromi, G. A Sequential Method to Prepare Polymorphs and Solvatomorphs of $[Fe(1,3\text{-bpp})_2](ClO_4)_2{\cdot}nH_2O$ (n = 0, 1, 2) with Varying Spin-Crossover Behaviour. *Chem. Eur. J.* **2016**, *22*, 12767.
(13) Chen, W.-B.; Leng, J.-D.; Wang, Z.-Z.; Chen, Y.-C.; Miao, Y.; Tong, M.-L.; Dong, W. Reversible crystal-to-crystal transformation from a trinuclear cluster to a 1D chain and the corresponding spin crossover (SCO) behavior change. *Chem. Commun.* **2017**, *53*, 7820.
(14) Chen, W.-B.; Chen, Y.-C.; Yang, M.; Tong, M.-L.; Dong, W. Water molecule induced reversible single-crystal to-single-crystal transformation between two trinuclear Fe(II) complexes with different spin crossover behavior. *Dalton Trans.* **2018**, *47*, 4307.
(15) Costa, J. S.; Rodríguez-Jiménez, S.; Craig, G. A.; Barth, B.; Beavers, C. M.; Teat, S. J.; Aromí, G. Three-Way Crystal-to-Crystal Reversible Transformation and Controlled Spin Switching by a Nonporous Molecular Material. *J. Am. Chem. Soc.* **2014**, *136*, 3869.
(16) Li, B.; Wei, R.-J.; Tao, J.; Huang, R.-B.; Zheng, L.-S.; Zheng, Z. Solvent-Induced Transformation of Single Crystals of a Spin-Crossover (SCO) Compound to Single Crystals with Two Distinct SCO Centers. *J. Am. Chem. Soc.* **2010**, *132*, 1558.
(17) Takahashi, K.; Okai, M.; Mochida, T.; Sakurai, T.; Ohta, H.; Yamamoto, T.; Einaga, Y.; Shiota, Y.; Yoshizawa, K.; Konaka, H.; Sasaki, A. Contribution of Coulomb Interactions to a Two-Step Crystal Structure Phase Transformation Coupled with a Significant Change in Spin Crossover Behavior for a Series of Charged FeII Complexes from 2,6-Bis(2-methylthiazol-4-yl)pyridine. *Inorg. Chem.* **2018**, *57*, 1277.
(18) Jain, S. L.; Slawin, A. M. Z.; Woollins, J. D.; Bhattacharyya, P. The Reactions of Elemental Iron with Dipicolinic Acid (H_2dipic) and Quinaldic Acid (Hquin) − X-ray Crystal Structures of $[C_5H_5NH][Fe(Dipic)(Hdipic)(C_5H_5N)_2]{\cdot}3C_5H_5N$, $[Fe_2(\mu\text{-}O)(Dipic)_2(C_5H_5N)_4]{\cdot}2C_5H_5N{\cdot}2H_2O$ and trans-$[Fe(Quin)_2(MeOH)_2]$. *Eur. J. Inorg. Chem.* **2005**, 721.
(19) Uhrecký, R.; Padělková, Z.; Moncol, J.; Koman, M.; Dlháň, L.; Titiš, J.; Boča, R. Synthesis, crystal structure, spectra and magnetic properties of new manganese(III) and iron(III) dipicolinate complexes. *Polyhedron* **2013**, *56*, 9.
(20) Thich, J. A.; Ou, C. C.; Powers, D.; Vasiliou, B.; Mastropaolo, D.; Potenza, J. A.; Schugar, H. J. Molecular Structure and Magnetic Properties of p-Dihydroxo-bis[2,6-pyridinedicarboxylato aquoiron-(III)] and μ-Dihydroxo-bis[4-hydroxo-2,6-pyridinedi carboxylatoa-quoiron(111)] Tetrahydrate. *J. Am. Chem. Soc.* **1976**, *98*, 1425.
(21) Spackman, M. A.; Jayatilaka, D. Hirshfeld surface analysis. *CrystEngComm* **2009**, *11*, 19.
(22) Jiang, P.; Peng, F.; Chen, Y. Temperature-induced single-crystal-to-single crystal transformation of a binuclear Mn(II) complex into a 1D chain polymer. *RSC Adv.* **2016**, *6*, 89192.
(23) Wendler, K.; Thar, J.; Zahn, S.; Kirchner, B. Estimating the Hydrogen Bond Energy. *J. Phys. Chem. A* **2010**, *114*, 9529.
(24) Llano-Tomé, F.; Bazán, B.; Urtiaga, M. K.; Barandika, G.; Fidalgo-Marijuan, A.; Fernández de Luis, R.; Arriortua, M. I. Water-induced phase transformation of a Cu(II) coordination framework with pyridine-2,5-dicarboxylate and di-2-pyridyl ketone: synchrotron radiation analysis. *CrystEngComm.* **2015**, *17*, 6346.
(25) Spek, A. L. PLATON Program. *Acta Cryst. D* **2009**, *65*, 148.
(26) Kahn, O. *Molecular Magnetism*; Wiley-VCH: New York, 1993.
(27) Engelhardt, L.; Luban, M. Simple models and powerful tools for seeking a comprehensive understanding of the magnetic properties of molecular magnets. *Dalton Trans.* **2010**, *39*, 4687.
(28) *Bruker. Program name(s)*; Bruker AXS Inc.: Madison, Wisconsin, 2012.
(29) *Bruker. Program name*; Bruker AXS Inc.: Madison, Wisconsin, 2001.
(30) Sheldrick, G. M. *Acta Cryst. C* **2015**, *71*, 3−8.
(31) Frisch, M. J.; Trucks, G. W.; Schlegel, H. B.; Scuseria, G. E.; Robb, M. A.; Cheeseman, J. R.; Scalmani, G.; Barone, V.; Mennucci, B.; Petersson, G. A.; Nakatsuji, H.; Caricato, M.; Li, X.; Hratchian, H. P.; Izmaylov, A.; Bloino, F. J.; Zheng, G.; Sonnenberg, J. L.; Hada, M.; Ehara, M.; Toyota, K.; Fukuda, R.; Hasegawa, J.; Ishida, M.; Nakajima, T.; Honda; Kitao, Y. O.; Nakai, H.; Vreven, T.; Montgomery, J. A., Jr.; Peralta, J. E.; Ogliaro, F.; Bearpark, M.; Heyd, J. J.; Brothers, E.; Kudin, K. N.; Staroverov, V. N.; Keith, T.; Kobayashi, R.; Normand, J.; Raghavachari, K.; Rendell, A.; Burant, J. C.; Iyengar, S. S.; Tomasi, J.; Cossi, M.; Rega, N.; Millam, J. M.; Klene, M.; Knox, J. E.; Cross, J. B.; Bakken, V.; Adamo, C.; Jaramillo, J.; Gomperts, R.; Stratmann, R. E.; Yazyev, O.; Austin, A. J.; Cammi, R.; Pomelli, C.; Ochterski, J. W.; Martin, R. L.; Morokuma, K.; Zakrzewski, V. G.; Voth, G. A.; Salvador, P.; Dannenberg, J. J.; Dapprich, S.; Daniels, A. D.; Farkas, Ö.; Foresman, J. B.; Ortiz, J. V.; Cioslowski, J.; Fox, D. J. *Gaussian 09*, revision C.01; Gaussian, Inc.: Wallingford, CT, 2010.
(32) Schäfer, A.; Horn, H.; Ahlrichs, R. Fully optimized contracted Gaussian basis sets for atoms Li to Kr. *J. Chem. Phys.* **1992**, *97*, 2571−2577.

DOI: 10.1021/acsomega.8b03400
ACS Omega 2019, 4, 8731−8738